Volume 13
Number 18
21 September 2025
Pages 4849-5222

Biomaterials Science

rsc.li/biomaterials-science

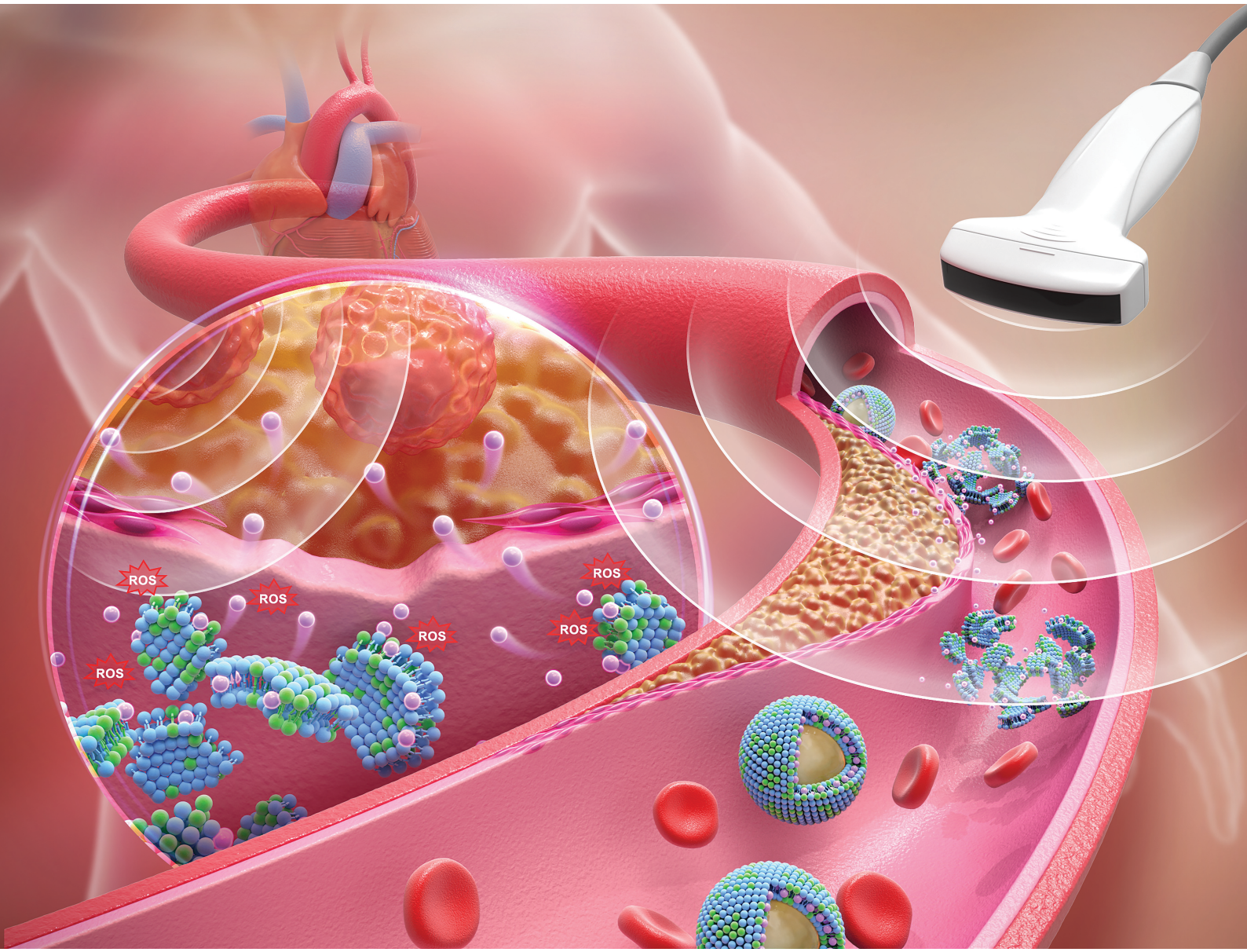

ISSN 2047-4849

ROYAL SOCIETY OF CHEMISTRY

PAPER
Yun Chen, Tingting Zheng *et al.*
A study of saponin-encapsulated ultrasound microbubbles Rb_3NPs@MBs for atherosclerosis targeted treatment

European Society for Biomaterials

Biomaterials Science

ROYAL SOCIETY OF CHEMISTRY

PAPER

View Article Online
View Journal | View Issue

Open Access Article. Published on 07 Caxah Alsa 2025. Downloaded on 06/05/2026 3:37:14 AM.
This article is licensed under a Creative Commons Attribution-NonCommercial 3.0 Unported Licence.

Check for updates

Cite this: *Biomater. Sci.*, 2025, **13**, 4984

A study of saponin-encapsulated ultrasound microbubbles Rb_3NPs@MBs for atherosclerosis targeted treatment†

Chunting Zhong, Jianhua Bai, Xiaoting Yang, Yiran Ji, Jiabao Huang, Xiao Tan, Xiaoyu Chen, LiJun Xing, Bingxuan Xu, Dianhuan Tan, Yun Chen* and Tingting Zheng *

Received 16th January 2025,
Accepted 5th May 2025

DOI: 10.1039/d5bm00078e

rsc.li/biomaterials-science

Atherosclerosis remains a leading disease posing significant threats to human health and life. Oxidative stress plays a critical role in the initiation of early atherosclerosis. Ginsenoside Rb_3 has been shown to exert potential therapeutic effects against atherosclerosis due to its antioxidant properties. However, its clinical utility remains constrained to the nanometer scale, offering insufficient targeting capability for atherosclerosis treatment. To address this limitation, we designed a novel Rb_3-loaded microbubble system Rb_3NPs@MBs. This microbubble system effectively encapsulates Rb_3 nanoparticles and, *via* ultrasound-targeted microbubble destruction (UTMD), facilitates their targeted accumulation in the aortic arch of atherosclerotic mice. Subsequently, Rb_3NPs@MBs reduce oxidative stress, attenuate endothelial cell apoptosis and foam cell formation, and ultimately diminish plaque development at the lesion site. This strategy holds promise as a therapeutic approach for atherosclerosis. These findings suggest that Rb_3NPs@MBs represent a promising therapeutic strategy for atherosclerosis.

1. Introduction

Cardiovascular disease (CVD) remains the leading cause of mortality among non-communicable diseases globally, exhibiting a high incidence rate.[1] Atherosclerosis (AS) is characterized by the formation of fibrofatty lesions within the arterial walls, leading to cardiovascular and cerebrovascular conditions such

Shenzhen Key Laboratory for Drug Addiction and Medication Safety, Department of Ultrasound, Institute of Ultrasonic Medicine, Peking University Shenzhen Hospital, Shenzhen Peking University-The Hong Kong University of Science and Technology Medical Center, Shenzhen, Guangdong Province 518036, P. R. China.
E-mail: yunchen@sphmc.org, kyzs_018@126.com

†Electronic supplementary information (ESI) available: Fig. S1–S8. See DOI: https://doi.org/10.1039/d5bm00078e

Chunting Zhong

Chunting Zhong is currently apostgraduate student majored in Biochemistry and Molecular Biology in Peking University Health Science Center. She received her bachelor degree in medical laboratory technology from Tianjin Medical University in 2022. She is currently focusing her research in targeted ultrasounic therapy for atherosclerosis.

Yun Chen

Prof. Yun Chen received her B.D. from Tongji Medical University in 1985 and M.D. from Guangzhou University of Chinese Medicine in 2006. She was a visiting scholar at Delaware Medical Heart Center and the Hong Kong Medical Authority in 1998 and 2000, respectively. She used to be the president of Peking University Shenzhen Hospital and she is a specialist in ultrasound diagnosis with over 30 years of clinical experience. Her present research mainly focuses on integrated ultrasound diagnosis and treatment.

This journal is © The Royal Society of Chemistry 2025

Open Access Article. Published on 07 Caxah Alsa 2025. Downloaded on 06/05/2026 3:37:14 AM.
This article is licensed under a Creative Commons Attribution-NonCommercial 3.0 Unported Licence.

as coronary heart disease and stroke. AS serves as the pathological foundation for the onset and progression of CVD.[2]

AS is a complex, multicellular, and staged disease that typically begins with apoptosis and dysfunction of endothelial cells.[3] When vascular endothelial cells are subjected to abnormal shear stress within blood vessels, the intracellular response to this disturbance results in the upregulation and increased activity of vascular cell adhesion molecule-1 (VCAM-1), as well as increased permeability to lipoproteins, particularly to low intensity lipoprotein (LDL) in the circulation.[4,5] LDL traverses the endothelial barrier and undergoes oxidation to form oxidized LDL (ox-LDL) within the intimal layer of blood vessels, where it accumulates.[6] Concurrently, monocytes are recruited from the bloodstream into the intimal region, where they differentiate into macrophages.[7,8] These macrophages take up ox-LDL and transform into foam cells, which accumulate and ultimately form plaques.[9] In summary, AS is a fibrofatty lesion in the arterial wall mediated by oxidative stress and inflammation.[10,11] At present, various symptomatic treatments are available for different clinical phenotypes of AS, including antithrombotic drugs, antilipemic agents, and anti-myocardial ischemia medications. Additionally, targeted therapies such as PCSK9 inhibitors and inflammatory factor monoclonal antibodies like Canakinumab have progressed to clinical trial stages.[12–16]

Ginseng, a traditional medicine in ancient China, is widely used for vascular protection in traditional medicine practices.[17–19] Saponin Rb_3, an extract derived from ginseng, has been investigated for its potential in treating AS due to its potent antioxidant effects.[20] Rb_3 can regulate energy metabolism and apoptosis in cardiomyocytes by activating the peroxisome proliferator-activated receptor alpha (PPARα) pathway, thereby enhancing cardiovascular function.[21,22] However, existing studies are limited to the incorporation of Rb_3 into nanosystems and the efficiency of targeted delivery is often suboptimal, particularly in regions with severe vascular plaques or specific localized areas.[23,24] In order to solve the problem of drug targeting, this study employed ultrasound-targeted microbubble destruction (UTMD) technology.[25–27] Typically, microbubbles—vacuole-like structures encapsulating a gas core—are utilized as ultrasound contrast agents.[28] By modifying the components of microbubbles, such as replacing the core gas with therapeutic gases like oxygen or carbon monoxide,[28,29] or by incorporating therapeutic agents (*e.g.*, genes, proteins, and nanomedicines),[30,31] therapeutic purposes can be achieved. UTMD facilitates the targeted explosion of microbubbles at specific sites under ultrasound guidance.[32] The resultant physical effects include the opening of tight junctions between cells, increased tissue permeability, enhanced cellular uptake of drugs, and augmented drug delivery efficiency.[33–40] As a non-invasive treatment modality,[41] UTMD has been validated for applications such as opening the blood–brain barrier,[42] enhancing the enhanced permeability and retention (EPR) effect in tumour therapy,[43,44] and treating AS.[45–48]

Therefore, in this study, a saponin-encapsulated microbubble system Rb_3NPs@MBs was constructed and combined with UTMD, so that the drug could be enriched in the targeted region of AS mice under ultrasound guidance. Using this drug delivery system, we verified the feasibility of RB_3NPs@MBs for reducing aortic plaques in AS mice and explored the related mechanism of RB_3NPs@MBs for the treatment of AS.

Tingting Zheng

Dr Tingting Zheng received her bachelor's and master's degrees from Beijing Normal University in 2006 and 2009, respectively. She obtained her PhD degree from Leiden University in 2014 and continued postdoctoral research at Wageningen University in the Netherlands. She is currently employed as a research fellow at Shenzhen PKU-HKUST Medical Center in P. R. China. Her research interests focus on the development and application of smart-targeting drug delivery system.

2. Materials and methods

2.1. Materials

1,2-Distearoyl-*sn-glycero*-3-phosphoethanolamine-*N*-[amino (polyethylene glycol)-2000] (DSPE-PEG2000) and 1,2-distearoyl-*sn-glycero*-3-phosphocholine (DSPC) were purchased from Avanti (816-94-4 & 474922-77-5, USA). Saponin Rb_3 was obtained from Chengdu Pufei (JOT-10260, China). Lipopolysaccharides (LPS) were obtained from Solarbio (L8880, China). Dulbecco's minimum essential medium (DMEM) and fetal bovine serum were purchased from Gibco (USA). Endothelial cell medium (ECM) was obtained from Sciencell (1001, USA). The mouse macrophage cell line (RAW264.7) was obtained from the Laboratory Center of Shenzhen University; the human umbilical vein endothelial cell line (HUVEC) was obtained from BeNa Culture Collection (BNCC378266, China).

2.2. Preparation and characterization of Rb_3NPs@MBs

DSPC and DSPE-PEG2000 were dissolved in chloroform at 7.90 mg ml^{-1} and 29.92 mg ml^{-1} respectively. Rb_3 was dissolved in a solvent mixture of chloroform and methanol (1 : 1, v/v) at a concentration of 2 mg ml^{-1}. To synthesize Rb_3NPs@MBs, 272 μl of DSPC, 30 μl of DSPE-PEG2000, and 500 μl of Rb_3 were combined in a round-bottom flask and subjected to rotary evaporation in a fume hood for 40 min to form a lipid film. The resultant lipid film was hydrated with 1 ml of phosphate-buffered saline (PBS) and ultrasonicated in a water bath maintained at 65 °C for 5–6 min. The hydrodynamic diameter of Rb_3NPs@Lipos was measured using dynamic light

Open Access Article. Published on 07 Caxah Alsa 2025. Downloaded on 06/05/2026 3:37:14 AM.
This article is licensed under a Creative Commons Attribution-NonCommercial 3.0 Unported Licence.

scattering (DLS) with a Zetasizer Nano (Malvern, England), and the structural morphology was characterized by transmission electron microscopy (TEM).

Subsequently, the Rb_3NPs@Lipos solution was transferred to a vial connected for gas exchange *via* syringes through rubber caps to produce Rb_3NPs@MBs. Initially, the gas within the vial was evacuated by vacuuming for 5 min, followed by the introduction of perfluoropropane (C_3F_8) for 1 min to facilitate gas mixing. To ensure complete gas exchange, this procedure was repeated 3–5 times. Subsequently, additional C_3F_8 was added, and the mixture was agitated using a shaker for 45 seconds to form Rb_3NPs@MBs. The size, particle size distribution, and concentration of Rb_3NPs@MBs were quantified using a particle analyzer (AccuSizer 780AD, USA) prior to structural examination under an optical microscope.

Conventional microbubbles (MBs) were prepared similarly to Rb_3NPs@MBs, excluding the addition of Rb_3. After establishing a standard curve for Rb_3 *via* ultraviolet (UV) spectrophotometry, uncoated and coated Rb_3 were separated by centrifuging the Rb_3NPs@MBs solution (5000 rpm for 10 min) in an ultrafiltration tube. The encapsulation efficiency and drug loading of Rb_3NPs@MBs were subsequently determined using UV spectrophotometry.

To assess blood compatibility, the hemolysis rate (HR) of Rb_3NPs@MBs after contact with blood was calculated. After the whole blood of fresh heparin sodium anticoagulated C57BL/6J mice was centrifuged and washed, the red blood cells were resuspended in a 2% concentration red blood cell suspension in PBS. According to the concentration gradient (10, 50, 100, and 1000 μg ml^{-1}), Rb_3NPs@MBs and the red blood cell suspension were gently mixed (volume ratio 1 : 1), and each concentration was divided into two groups: the UTMD group (given ultrasound operation) and the free group (without ultrasound operation), and incubated for 1 h at 37 °C. NS and the red blood cell suspension (volume ratio 1 : 1) were used as negative controls, and ddH_2O and the red blood cell suspension (volume ratio 1 : 1) were used as positive controls. The ultrasonic conditions were as follows: output frequency: 1.0 MHz; duty cycle: 20%; and pulse frequency: 100 Hz. The output sound intensity was 100 mW cm^{-2}. The time was 1 min. At the end of the incubation, the mixture was centrifuged at 3000 rpm for 10 min and the supernatant was removed. The supernatant was transferred to a 96-well plate, and the absorbance value at the specific wavelength of 541 nm of hemoglobin was measured using a microplate reader. Each well was set up with three repeat wells. The HR was calculated using the following formula:

$$\mathrm{HR}\,(\%) = \frac{\mathrm{OD_{test}} - \mathrm{OD_{negative\ control}}}{\mathrm{OD_{positive\ contorl}} - \mathrm{OD_{negative\ \ contorl}}} \times 100\%.$$

2.3. Evaluation of the therapeutic effect *in vitro*

RAW264.7 cells were cultured in DMEM with 10% FBS and 1% penicillin/streptomycin (1% penicillin and 1% streptomycin). HUVEC cells were cultured in ECM with 10% FBS, 1% ECGs, and 1% penicillin/streptomycin (1% penicillin and 1% streptomycin). Cells were maintained in an incubator at 37 °C under a humidified atmosphere and 5% CO_2.

2.3.1. *In vitro* biocompatibility assay of Rb_3NPs@MBs. To evaluate cell viability, RAW264.7 cells and HUVEC cells were seeded in 96-well plates at a density of 2×10^4 cells per well. The cells were treated with varying concentrations of Rb_3NPs@MBs (0, 1, 5, 10, 25, 50, and 100 μg ml^{-1}) in combination with UTMD. Ultrasound was induced using a LIPUSTIM® device (SX Ultrasonic, China) with the following parameters: frequency of 1.0 MHz, duty cycle of 50%, pulse rate of 1000 Hz, intensity of 500 mW cm^{-2}, and duration of 3 min. Subsequently, the cells were incubated for 24 h. Cell viability across different concentration groups was then assessed using the CCK-8 assay kit (Biosharp, China).

2.3.2. Selection of *in vitro* Rb_3NPs@MBs therapeutic concentrations. To determine the optimal concentration of Rb_3NPs@MBs to be used in *in vitro* experiments, confocal microscopy was utilized to evaluate the effect of varying drug concentrations on the scavenging of LPS-induced reactive oxygen species (ROS). After 24 h of incubation, the original medium was aspirated, and the cells were treated with different concentrations of Rb_3NPs@MBs (0, 5, 10, 25, and 50 μg ml^{-1}) in combination with UTMD using the following settings: frequency of 1.0 MHz, duty cycle of 20%, pulse rate of 100 Hz, intensity of 100 mW cm^{-2}, and duration of 1 min. Subsequently, the cells were co-cultured with 1 μg ml^{-1} LPS for 6 hours. After treatment, the cells were collected and incubated at 37 °C for 30 min using 10 μmol L^{-1} of ROS probes (Invitrogen, USA). Then, the cells were stained with DAPI (Beyotime, China) for observation under a confocal microscope (LSM719, Carl Zeiss Jena, Germany).

2.3.3. Assessment of ultrasound enhanced cellular uptake. To explore whether UTMD promoted the uptake of Rb_3NPs@MBs by RAW264.7 cells and HUVEC cells, Nile red (NR) fluorescent dye was used to replace Rb_3NPs to prepare fluorescent microbubbles NRNPs@MBs. Flow cytometry was used to quantitatively measure the uptake of fluorescence by cells at different time points.

The NRNPs concentration, NRNPs@MBs preparation, and subsequent characterization of the NRNPs@MBs were the same as that in section 2.2. RAW264.7 cells and HUVEC cells in good growth condition were plated in 6-well plates, and 2 ml of 1×10^5 ml^{-1} cell suspension was added to each well and cultured for 24 h. The cells were divided into the control group, NRNPs group (10 μg ml^{-1}), and NRNPs@MBs + UTMD (10 μg ml^{-1}) group, and the UTMD parameters were the same as those in section 2.3.2. After treatment, the cells were collected at different time points (30 min, 1 h, 3 h, 6 h, 12 h, and 24 h), washed with PBS three times, and centrifuged at 1000 rpm for 5 min each time. After the last wash, the cells were resuspended in 500 μl PBS for flow cytometry, and the fluorescence channel was the PE channel.

2.3.4. Examination of DiI-ox-LDL uptake of RAW264.7 cells. RAW264.7 cells were seeded in a confocal dish at a density of 1×10^5 cells per well. After 24 h of culture, the original medium was removed. The cells were divided into five

 This journal is © The Royal Society of Chemistry 2025

Open Access Article. Published on 07 Caxah Alsa 2025. Downloaded on 06/05/2026 3:37:14 AM.
This article is licensed under a Creative Commons Attribution-NonCommercial 3.0 Unported Licence.

groups, namely, the control group, LPS group (1 μg ml^{-1} of LPS), MBs + UTMD group (1 μg ml^{-1} of LPS and 10 μg ml^{-1} of MBs + UTMD), Rb_3NPs group (1 μg ml^{-1} of LPS and 10 μg ml^{-1} of Rb_3NPs, which was dissolved in normal saline), and Rb_3NPs@MBs + UTMD group (1 μg ml^{-1} LPS and 10 μg ml^{-1} Rb_3NPs@MBs + UTMD); the setting of UTMD was the same as that in section 2.3.2. After 24 h of treatment according to different groups, the original medium was removed, and the medium containing 40 μg ml^{-1} Dil-ox-LDL (Guangzhou Yiyuan Biotechnologies, China) was added and incubated for 6 h. Then, the dishes were washed three times with PBS, and stained with DAPI for observation with a confocal microscope.

2.3.5 Measurement of apoptosis of HUVEC cells. HUVEC cells were seeded in a 6-well plate at a density of 2×10^5 cells per well and incubated overnight. The cells were divided into five groups same as those in section 2.3.4, namely, the control group, LPS group, MBs + UTMD group, Rb_3NPs group, and Rb_3NPs@MBs + UTMD group; the setting of UTMD was the same as that in section 2.3.4. After 24 h, the cells were collected and analyzed using an annexin V-FITC/PI apoptosis detection kit (Servicebio, China) according to the protocol. Then a flow cytometer (cytoFLEX S, Beckman Coulter, USA) was used to detect cell apoptosis.

2.3.6 JC-1 staining to assess the degree of oxidative stress in HUVEC cells. HUVEC cells were seeded in a confocal dish at a density of 1×10^5 cells per well and cultured for 24 h. After the cells were grouped and treated as described in section 2.3.4, they were cultured for an additional 24 h. Staining was performed according to the instructions of the JC-1 staining kit (Solarbio, China). Finally, the cells stained with DAPI were observed under a confocal microscope.

2.3.7 Flow cytometry-based measurement of intracellular ROS levels of RAW264.7 cells. RAW264.7 cells were seeded in a 6-well plate at a density of 2×10^5 cells per well and incubated overnight. The cells were divided into five groups and treated in the same way as in section 2.3.4. The treatment of cells incubated with ROS probes was similar to that in section 2.3.2, except that the cells incubated with ROS probes were centrifuged (1000 rpm, 5 min) and washed with PBS 3 times to remove the non-specifically bound probes as much as possible. The cells were then resuspended in 500 μl of PBS and subjected to flow assays.

2.3.8 Determination of intracellular superoxide dismutase (SOD) activity and glutathione (GSH) levels. RAW264.7 cells and HUVEC cells were spread onto 6-well plates, and the cells were grouped and processed according to the process discussed in section 2.3.4. Then, the cells were harvested and sonicated to obtain cellular proteins after 24 h of culture. The total protein concentration of the resulting supernatant was determined using a bicinchoninic acid protein assay kit (BCA, Solarbio, China). Then experiments were carried out according to the instructions of the SOD and GSH assay kit (Nanjing Jiancheng Bioengineering Institute, China) and the results were measured by using a microplate reader. Finally, the corresponding SOD and GSH levels were calculated using the concentration of total protein and the results of the microplate reader.

2.3.9 Western blotting. HUVEC cells were seeded in 6-well plates and grouped and treated as described in section 2.3.5. After 24 h, proteins from cultured cells were collected and lysed with RIPA buffer. Total protein concentration was determined by the BCA assay. Special care was taken so that the collected proteins were not heat-denatured. Proteins were separated by 6% sodium dodecyl sulfate polyacrylamide gel electrophoresis (SDS-PAGE) and transferred to polyvinylidene difluoride (PVDF) membranes. After blocking with 5% nonfat milk in tribuffered saline containing 0.05% Tween 20 (TBST) for 1 h at room temperature, the membranes were incubated with anti-VCAM-1 antibodies (11444-1-AP, Proteintech) overnight at 4 °C. The cells were then incubated with secondary HRP-conjugated antibodies for 1 h at room temperature. After addition of the ECL substrate, images were acquired using an Amersham imager.

2.4 Evaluation of the therapeutic effect *in vivo*

5–6 week old male C57BL/6J mice and $ApoE^{-/-}$ mice were purchased from Guangdong Yaokang Biological Technology (China). This study was approved by the Experimental Animal Center of Shenzhen PKU-HKUST Medical Center. All experimental procedures were performed in accordance with the National Institutes of Health Guide for Care and Use of Laboratory Animals and according to the institutional animal experimental ethical guidelines. $ApoE^{-/-}$ mice were fed a high-fat diet (1.25% cholesterol), C57BL/6J mice were fed a normal diet, and all mice were provided free access to water. $ApoE^{-/-}$ mice were fed for 12 weeks to establish an AS model.

2.4.1 Safety evaluation. For safety evaluation, the treatment regimen consisted of administrations once every two days over a two-week period of C57BL/6J and AS mice. Ultrasound treatment was performed using a Vevo 2100 ultra-high-frequency small animal ultrasound imager (Visual Sonics, Canada) with the following parameters: contrast gain of 30 dB, frequency of 18 MHz, and mechanical index (MI) ranging from 0.6 to 0.8. Ultrasonic bursts occurring every 5–10 seconds were sustained for a total duration of 1 min per session. The UTMD treatment was given at the position of the aortic arch; all mice were treated by tail vein injection with a dosage of 30 mg kg^{-1} drug. At the end of the treatment period, major organs and blood samples were collected for subsequent analysis to assess potential safety and physiological impacts.

2.4.2 Validation of aortic arch enrichment and 24 h metabolism of Rb_3NPs@MBs + UTMD. To validate that the combined application of Rb_3NPs@MBs and UTMD facilitates targeted disruption and drug enrichment within the target area, *in vivo* small animal imaging was conducted using an IVIS Lumina LT system (PerkinElmer). Since Rb_3NPs@MBs are inherently non-fluorescent, Cy7.5 maleimide (MedChemExpress, USA) was employed as a fluorescent substitute for Rb_3 to fabricate Cy7.5@MBs. The experiments were divided into three groups (n = 3): control group (normal saline), Cy7.5 group (Cy7.5-NS), and Cy7.5@MBs + UTMD group (Cy7.5@MBs and UTMD). The drug dosage and UTMD procedures for all experimental groups were consistent with those described in section 2.4.1.

Open Access Article. Published on 07 Caxah Alsa 2025. Downloaded on 06/05/2026 3:37:14 AM.
This article is licensed under a Creative Commons Attribution-NonCommercial 3.0 Unported Licence.

One hour later, the distribution of Cy7.5 in mice was observed. After 24 hours, the mice were dissected, and the vital organs were taken to observe the residue of Cy7.5 in the organs.

In order to further verify the targeting function of UTMD, another 6 mice were selected for the same operation. After Cy7.5@MBs was circulated in the mice for 1 hour, the mice were sacrificed and the aortic tissues were collected for frozen section, stained with DAPI, and confocal microscopy was used to observe the enrichment of Cy7.5 in the plaque at the targeted site of ultrasound.

2.4.3 Rb_3NPs@MBs + UTMD targeted therapy in atherosclerotic model mice. The mice with established AS were divided into six groups (n = 8): normal control group, model group, MBs + UTMD group (Sonovue microbubbles and UTMD), simvastatin (SV) group (SV-NS solution), Rb_3NPs group (Rb_3NPs-NS solution), and Rb_3NPs@MBs + UTMD group (Rb_3NPs@MBs and UTMD). The normal control group and the model group were given normal saline. After accurately locating the aortic arch using ultrasound imaging, the drug was administered to the mice *via* tail vein injection. UTMD was subsequently performed once the microbubbles had adequately circulated within the blood vessels and vascular contrast was enhanced. The drug dosage and UTMD procedures for all experimental groups were consistent with those described in section 2.4.1.

Following the treatment period, the mice were subjected to a 12-hour fasting regimen before being euthanized and dissected. The serum biomarker detection was performed by Servicebio (Wuhan, China).

2.5 Statistical analysis

Data are indicated as mean ± SD. Paired t-test or ANOVA was carried out as indicated to establish the statistical differences. All the statistical computations were performed using the GraphPad Prism software. P-Values <0.05 were considered to indicate significant differences: $^{*}P < 0.05$, $^{**}P < 0.01$, $^{***}P < 0.001$, $^{****}P < 0.0001$.

3. Results

3.1 Characterization of Rb_3NPs@Lipos and Rb_3NPs@MBs

In this study, Rb_3NPs@Lipos were prepared using the classical film hydration technique, and their particle size and zeta potential were determined by dynamic light scattering (DLS) (Fig. 1A & Fig. S1B†).[49] The results showed that the hydrated particle size of Rb_3NPs@Lipos was about 165.7 ± 21.52 nm. Transmission electron microscopy (TEM) results revealed that Rb_3NPs@Lipos exhibited the classic circular and homogeneous liposomal morphology (Fig. 1B). These findings indicate that the prepared Rb_3NPs@Lipos possess uniform size distribution and can be employed for subsequent microbubble fabrication.

Following gas displacement of the Rb_3NPs@Lipos solution, Rb_3NPs@MBs were generated. The particle size and concentration of Rb_3NPs@MBs were evaluated using a particle size analyser (PSS). To minimize the risk of vascular occlusion, the size of microbubbles should be below 10 μm, preferably near the diameter of erythrocytes (~7.2 μm).[50] As shown in Fig. 1C, Rb_3NPs@MBs exhibited a uniform particle size of 1.70 ± 0.036 μm with a concentration of 2.1×10^9 ml^{-1}, and a normally distributed particle size profile. Optical microscopy revealed that Rb_3NPs@MBs exhibited the classical hollow spherical structure with uniform dispersion (Fig. 1D). The zeta potential of Rb_3NPs@MBs was −2.909 ± 0.636 mV, bigger than that of Rb_3NPs@Lipos (Fig. S1B†). Stability assessments over a 72 h period (Fig. S2†) showed that the concentration of Rb_3NPs@MBs remained on the order of 1×10^8 mL^{-1}, suggesting that the Rb_3NPs@MBs system is stable.

Then, using an ultraviolet spectrophotometer, we found that the encapsulation efficiency of Rb_3NPs@MBs was 88.48%, and the drug loading was 22.12%, respectively. In addition, to evaluate the compatibility of Rb_3NPs@MBs in contact with blood, the hemolysis rate test results showed that Rb_3NPs@MBs has excellent blood compatibility (HR% <5%) at concentrations ≤100 μg ml^{-1}, and its ultrasonic response characteristics do not induce additional hemolytic damage, which meets the biosafety requirements of intravenous drug delivery systems (Fig. S3†). Then, using an ultraviolet spectrophotometer, we found the encapsulation efficiency of Rb_3NPs@MBs to be 88.48% and the drug loading to be 22.12%, respectively. Furthermore, the assessments over a 72 h period (Fig. S2†) showed that the concentration of Rb_3NPs@MBs remained on the order of 1×10^8 ml^{-1}, suggesting that the Rb_3NPs@MBs system is stable.

In summary, we successfully fabricated Rb_3NPs@MBs with diameters of 1.70 μm, which demonstrated uniform size distribution, stability, and homogeneous dispersion.

3.2 Ultrasound enhanced cellular uptake

For cellular uptake experiments, cells were treated with 10 μg ml^{-1} NRNPs and 10 μg ml^{-1} NR@MBs, and then collected at 4 time points (30 min, 1 h, 3 h, and 6 h) to observe the cellular uptake of the dye. The results are shown in Fig. 2. Fig. 2A–C shows the cellular uptake results of RAW264.7 cells. It can be seen that UTMD promoted the uptake of NR by cells within 30 min–6 h after treatment, and the fluorescence intensity of cells was significantly stronger than that of the NRNPs group. Fig. 2D–F show the cellular uptake results of HUVEC cells. It can be seen that in 30 min–6 h, ultrasound was also observed to promote the absorption of NR in HUVEC cells.

However, after careful analysis of the comparative data, we found that the fluorescence of the NRNPs group in RAW264.7 cells increased with time, but this phenomenon was not observed in HUVEC cells. Considering that the drug action time is usually 24 hours in *in vitro* experiments, in order to explore the reason for the fluorescence growth of RAW264.7 cells, we continued to set a longer time curve to observe the fluorescence uptake of cells, and the results are shown in Fig. S4.† The fluorescence uptake of RAW264.7 cells increased with time, and there was no statistically significant difference

 This journal is © The Royal Society of Chemistry 2025

Open Access Article. Published on 07 Caxah Alsa 2025. Downloaded on 06/05/2026 3:37:14 AM.
This article is licensed under a Creative Commons Attribution-NonCommercial 3.0 Unported Licence.

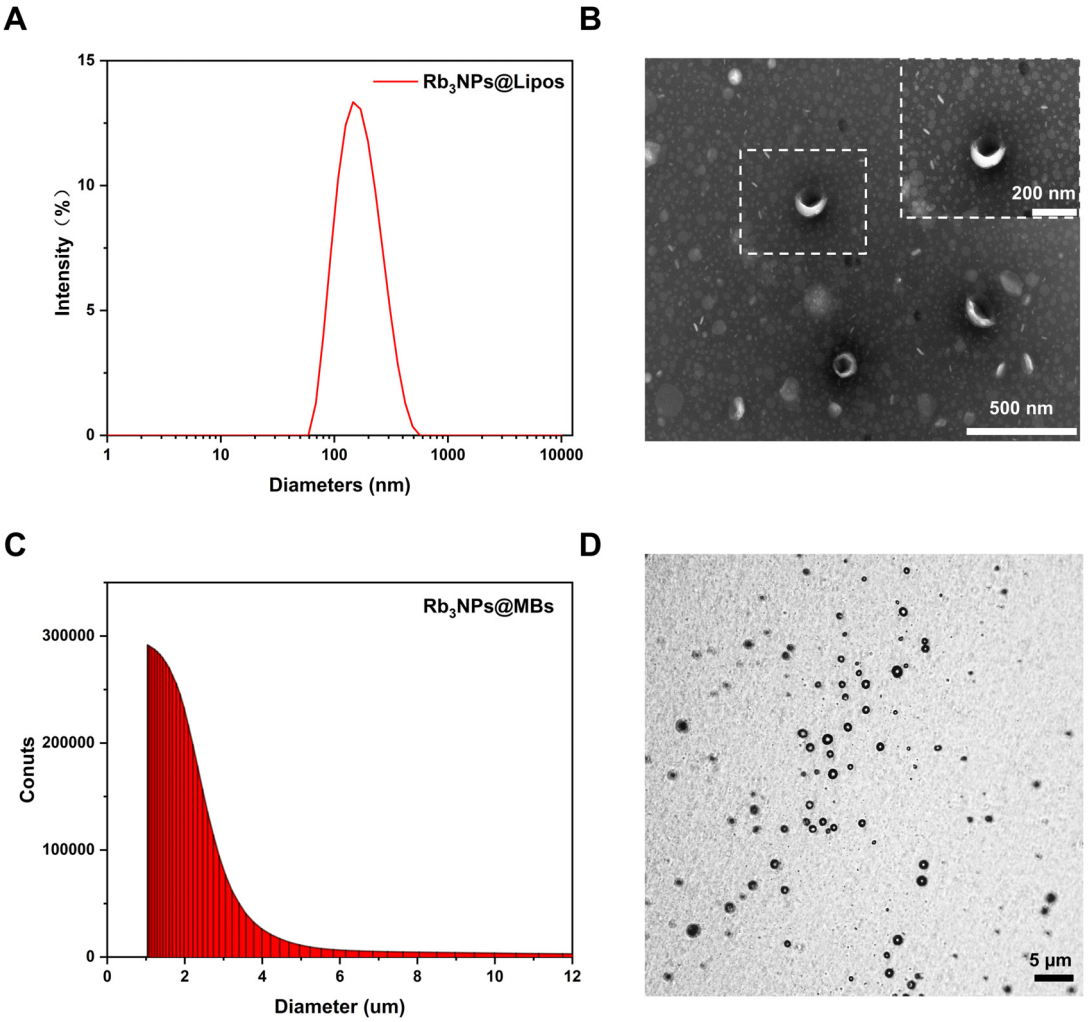

Fig. 1 The characterization of Rb_3NPs@Lipos and Rb_3NPs@MBs. (A) The particle size of Rb_3NPs@Lipos was measured by DLS. (B) The morphological structure of Rb_3NPs@Lipos was observed by TEM. (C) The concentration and size distribution of Rb_3NPs@MBs were measured by PSS. (D) The structures of Rb_3NPs@MBs were observed light microscope.

in fluorescence intensity between the NRNPs group and the NRNPs@MBs + UTMD group at 24 h.

In summary, UTMD promoted the uptake of fluorescence, and it can also be assumed that when NR was replaced by Rb_3NPs, UTMD would also promote the uptake of the drug.

3.3 The therapeutic effect of Rb_3NPs@MBs *in vitro*

In order to elucidate the therapeutic effects of the prepared formulation on early AS events, RAW264.7 cells and HUVECs were employed *in vitro*. Additionally, a microbubble-only (MBs) group was included to confirm that any therapeutic benefits were attributable to Rb_3NPs@MBs rather than the mechanical effects associated with microbubble destruction.

First, a CCK-8 assay was performed to assess the impact of UTMD combined with Rb_3NPs@MBs on cell viability. As a widely used assay reflecting proliferative capacity, the CCK-8 results revealed that the combination of UTMD and Rb_3NPs@MBs at concentrations ranging from 1 to 100 μg ml^{-1} did not significantly affect RAW264.7 cells and HUVEC viability (Fig. 3A).

Subsequently, confocal microscopy was utilized to examine the intracellular ROS-scavenging capacity of Rb_3NPs@MBs at various concentrations in order to determine the optimal concentration for *in vitro* experiments. Here, LPS was used to induce an inflammatory response, reflecting its well-established role as a cost-effective, highly reproducible stimulus for creating *in vitro* inflammatory disease models, including those relevant to AS.[51]Confocal images showed that when the treatment of Rb_3NPs@MBs combined with UTMD was absent (0 μg ml^{-1}, only LPS treatment), green fluorescence indicative of ROS was most pronounced. Among the 5–50 μg ml^{-1} Rb_3NPs@MBs treatment groups, the 10 and 25 μg ml^{-1} conditions demonstrated the most substantial reduction in fluorescence (Fig. 3B), with subsequent ImageJ-based quantitative analysis corroborating that 10 and 25 μg ml^{-1} yielded optimal ROS-scavenging activity (Fig. 3C). Based on the principle of

Open Access Article. Published on 07 Caxah Alsa 2025. Downloaded on 06/05/2026 3:37:14 AM.
This article is licensed under a Creative Commons Attribution-NonCommercial 3.0 Unported Licence.

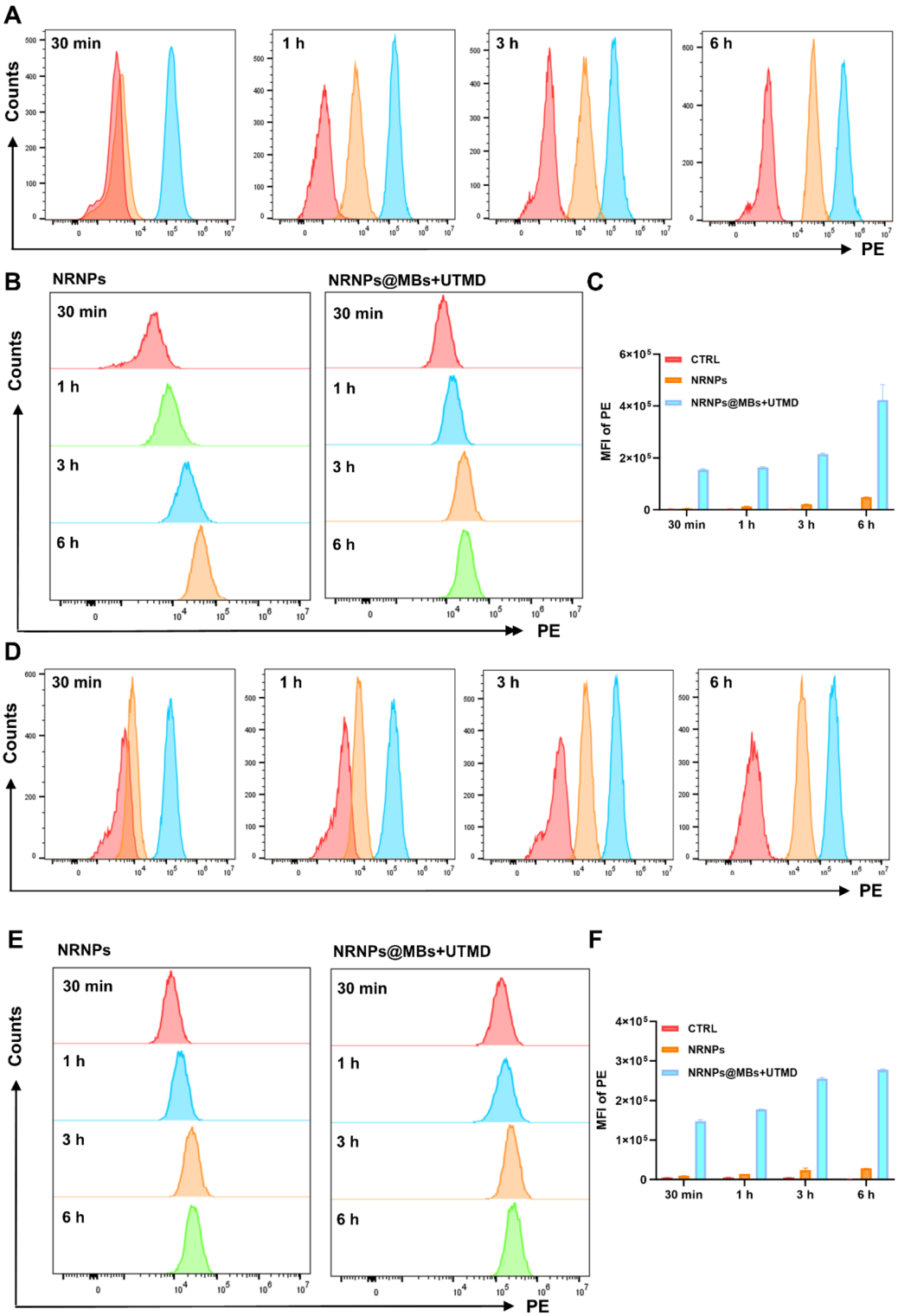

Fig. 2 Cellular uptake at different time points was determined by flow cytometry. (A) Fluorescence flow diagram of RAW264.7 cells at 30 min, 1 h, 3 h, and 6 h, and the group color corresponds to the legend color in (C). (B) Comparison of fluorescence flow images of RAW264.7 cells with the NRNPs group and NRNPs@MBs + UTMD group at different time points. (C) Quantitative analysis of flow fluorescence intensity in (A) (n = 3). (D) Fluorescence flow diagram of HUVEC cells at 30 min, 1 h, 3 h, and 6 h, and the grouping colors correspond to the legend colors in (F). (E) Comparison of fluorescence flow images of HUVEC cells at different time points between the NRNPs group and the NRNPs@MBs + UTMD group. (F) Quantitative analysis of flow fluorescence intensity in (D) (n = 3).

This journal is © The Royal Society of Chemistry 2025

Open Access Article. Published on 07 Caxah Alsa 2025. Downloaded on 06/05/2026 3:37:14 AM.
This article is licensed under a Creative Commons Attribution-NonCommercial 3.0 Unported Licence.

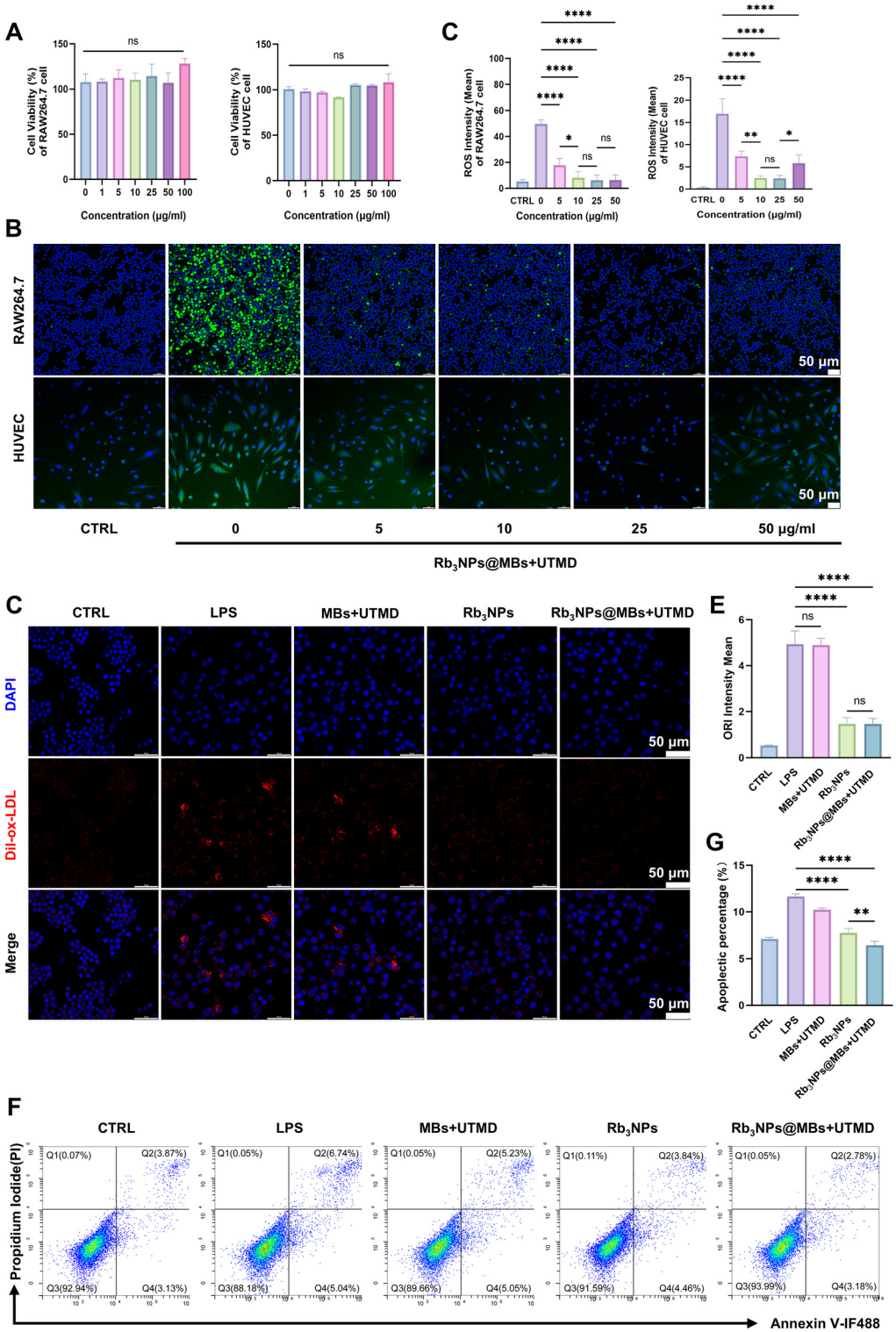

Fig. 3 The therapeutic effect of Rb_3NPs@MBs *in vitro*. (A) The effect on cell viabilities were evaluated by the CCK-8 assay (n = 3). The concentration of Rb_3NPs@MBs from 1 to 100 μg ml^{-1}. (B) Confocal microscopy was used to observe intracellular ROS fluorescence intensity. Green fluorescence represents ROS and blue fluorescence represents cell nuclei. Scale bar = 50 μm. (C) Quantification of ROS fluorescence intensity in (B) (n = 3). (D) The uptake of Dil-ox-LDL by RAW264.7 cells was observed by confocal microscopy. Red fluorescence represents Dil-ox-LDL, and blue fluorescence represents the cell nucleus. Scale bar = 50 μm. (E) Quantitative analysis of Dil-ox-LDL fluorescence intensity in (D) (n = 3). (F) The apoptosis of HUVEC cells was analyzed by flow cytometry. (G) Statistical analysis of the proportion of apoptosis in (F) (n = 3).

Open Access Article. Published on 07 Caxah Alsa 2025. Downloaded on 06/05/2026 3:37:14 AM.
This article is licensed under a Creative Commons Attribution-NonCommercial 3.0 Unported Licence.

administering the minimum effective dose, 10 μg ml^{-1} was chosen for all subsequent *in vitro* experiments.

To investigate whether Rb_3NPs@MBs could diminish ox-LDL uptake by RAW264.7 cells and thereby attenuate foam cell formation, cells were incubated with Dil-ox-LDL, an oxidized low-density lipoprotein labeled red fluorescence.[52] Confocal microscopy and quantitative fluorescence analysis revealed that MBs combined with UTMD did not significantly reduce Dil-ox-LDL uptake compared to the LPS-only group. In contrast, both the Rb_3NPs and the Rb_3NPs@MBs + UTMD treatments exhibited a marked decrease in red fluorescence (Fig. 3D and E), indicating a significant inhibition of ox-LDL uptake and foam cell formation. Notably, no statistically significant difference was observed between the Rb_3NPs and Rb_3NPs@MBs + UTMD groups. Then, the effect of Rb_3NPs@MBs on HUVEC apoptosis was examined. Flow cytometry demonstrated that both Rb_3NPs and Rb_3NPs@MBs + UTMD treatments reduced LPS-induced HUVEC apoptosis, with a more pronounced anti-apoptotic effect observed in the Rb_3NPs@MBs + UTMD group (Fig. 3F and G). These findings suggest that the combination of Rb_3NPs@MBs and UTMD effectively mitigates two hallmarks of early AS events—foam cell formation and endothelial cell apoptosis.

Moreover, the therapeutic benefit in HUVECs was superior when Rb_3NPs were delivered *via* MBs combined with UTMD relative to Rb_3NPs alone.

3.4 Rb_3NPs@MBs reduce oxidative stress in cells

Numerous studies have demonstrated that oxidative stress plays a pivotal role in the pathogenesis of AS. As an inflammatory disease, the entire progression of AS is often accompanied by an imbalance between intracellular oxidative and antioxidant mechanisms. To determine whether Rb_3NPs@MBs can modulate key cellular events through the reduction of oxidative stress, we performed a series of experiments to assess the oxidative stress levels in HUVECs and RAW264.7 cells.

First, in HUVECs, we assessed mitochondrial membrane potential ($\Delta\Psi_m$) using JC-1 staining. Mitochondria constitute the primary center of cellular energy and metabolism, with the mitochondrial respiratory chain serving as a principal source of reactive oxygen species (ROS).[53] The extent of mitochondrial mass is closely linked to ROS levels, and the decline in $\Delta\Psi_m$ reflects mitochondrial impairment. Under conditions of high mitochondrial membrane potential, the JC-1 dye accumulates within the mitochondrial matrix, forming aggregates that exhibit red fluorescence. Conversely, when the membrane potential is low, JC-1 remains in its monomeric form and produces green fluorescence. In this study, we observed that the green fluorescence intensity in the LPS group was comparable to that of the CCCP (positive control) and MBs + UTMD groups, whereas the Rb_3NPs@MBs + UTMD groups displayed markedly weaker green fluorescence (Fig. 4A). These findings indicate that Rb_3NPs@MBs + UTMD effectively mitigated the LPS-induced reduction in mitochondrial membrane potential in HUVECs.

In RAW264.7 cells, intracellular ROS levels were quantified by flow cytometry. As shown in Fig. 4B and C, the MBs + UTMD treatment alone did not attenuate LPS-induced ROS generation, while both Rb_3NPs and Rb_3NPs@MBs + UTMD substantially reduced ROS levels. This result is consistent with our previous observations. Notably, no significant difference was detected between the Rb_3NPs and Rb_3NPs@MBs + UTMD groups in terms of ROS suppression.

Finally, we measured superoxide dismutase (SOD) and glutathione (GSH) levels in HUVECs and RAW264.7 cells using commercial assay kits. SOD is a major antioxidant enzyme responsible for catalyzing the dismutation of superoxide anion radicals (O_2^-) into oxygen and hydrogen peroxide (H_2O_2), while GSH is a key antioxidant that directly scavenges free radicals and participates in multiple antioxidant reactions. Intracellular antioxidant capacity can therefore be evaluated by measuring both SOD and GSH. In HUVECs, the Rb_3NPs@MBs + UTMD group exhibited significantly higher SOD and GSH levels compared with the LPS group, and this effect exceeded that observed in the Rb_3NPs group. Similarly, in RAW264.7 cells, Rb_3NPs@MBs + UTMD markedly enhanced SOD and GSH content relative to the LPS group, although no statistically significant difference was found between the Rb_3NPs and Rb_3NPs@MBs + UTMD groups (Fig. 4D).

Collectively, these data suggest that Rb_3NPs@MBs effectively mitigate oxidative stress in both RAW264.7 and HUVEC cells. However, whether the combined delivery of Rb_3NPs@MBs and UTMD confers additional therapeutic benefits in RAW264.7 cells requires further investigation.

3.5 Biodistribution of microbubbles combined with UTMD *in vivo*

The effects of 2 weeks Rb_3NPs@MBs + UTMD on liver and kidney biochemical indicators (ALT, AST, BUN, and CRE), blood cell count (white blood cell count, neutrophil count, lymphocyte count, and monocyte count) and important organs (heart, liver, spleen, lungs, and kidneys) of mice were not different from those of normal mice. We then set out to explore whether UTMD similarly promotes drug absorption *in vivo* (Fig. S7†). Ultrasound is a commonly used imaging modality, particularly valuable for vascular imaging. It enables the visualization of multidimensional parameters, such as hemorheology, vascular plaque formation, and vascular stenosis.[54] Among various ultrasound-based techniques, UTMD has emerged as a promising drug delivery strategy, owing to its safety, noninvasive nature, ease of operation, and high targeting efficiency.

To evaluate the *in vivo* targeting efficiency of UTMD and the distribution and metabolism of microbubbles, we substituted Rb_3NPs with Cy7.5 (a fluorescent probe) and prepared Cy7.5@MBs following the same protocol and concentration used for Rb_3NPs@MBs. The UTMD-induced disruption process of Cy7.5@MBs is depicted in Scheme 1, while the operational details are demonstrated in Video 1 of the ESI.† Briefly, after locating the aortic arch *via* ultrasound, Cy7.5@MBs were administered through the tail vein of AS mice. When the microbubbles had adequately filled the vessels and enhanced the ultrasound

 This journal is © The Royal Society of Chemistry 2025

Open Access Article. Published on 07 Caxah Alsa 2025. Downloaded on 06/05/2026 3:37:14 AM.
This article is licensed under a Creative Commons Attribution-NonCommercial 3.0 Unported Licence.

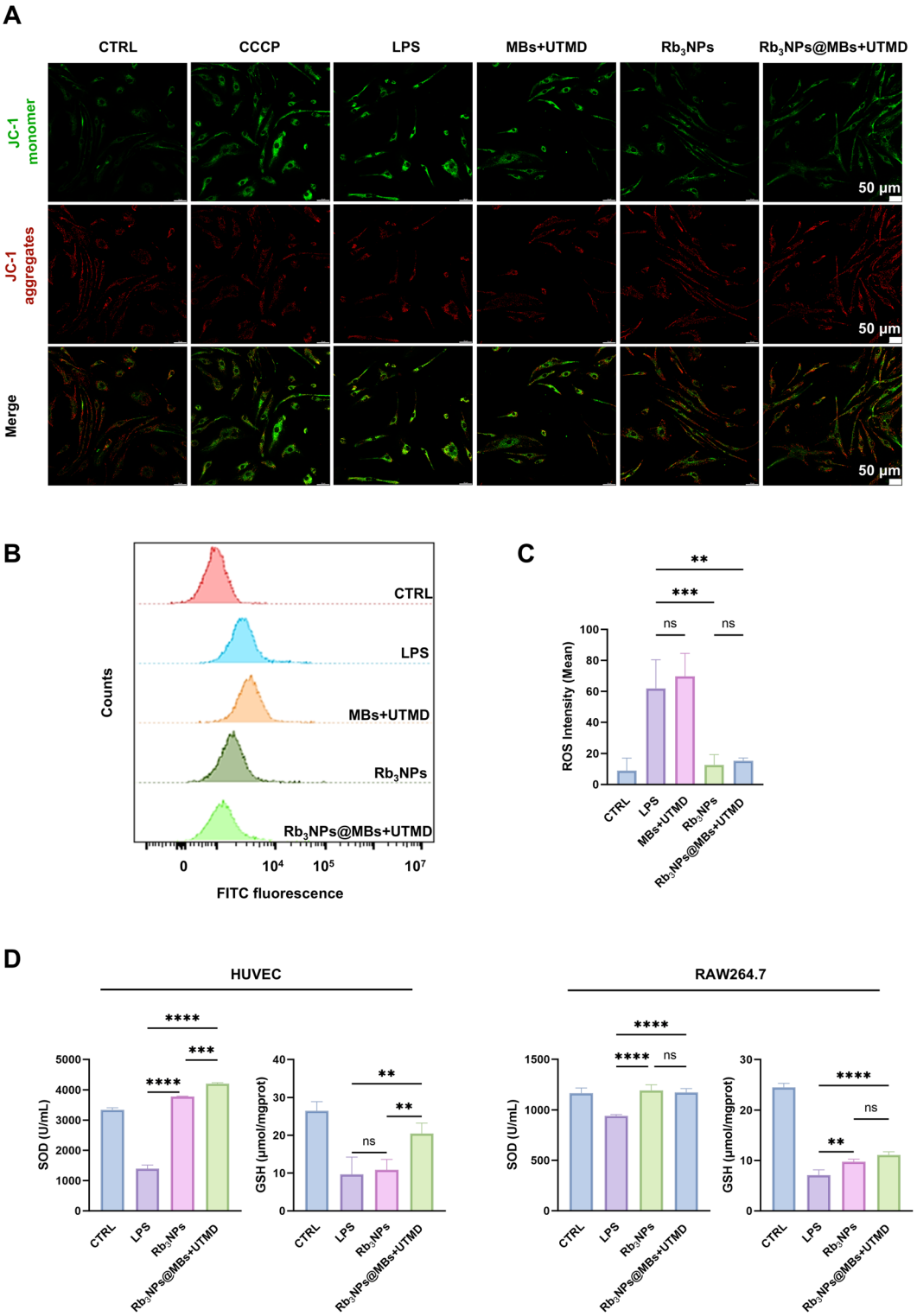

Fig. 4 Rb_3NPs@MBs reduce oxidative stress in cells. (A) JC-1 staining of HUVEC cells. The CCCP group is the positive control group. Green fluorescence represents the JC-1 monomer and red fluorescence represents JC-1 aggregates (n = 3). Scale bar = 50 μm. (B) ROS flow analysis in RAW264.7 cells. (C) Quantitative analysis of the data in B (n = 3). (D) SOD and GSH oxidation factors in HUVEC cells and RAW264.7 cells (n = 3).

contrast, UTMD was applied at the aortic arch. One hour later, *in vivo* fluorescence imaging was performed (n = 3), and after 24 hours of circulation, the major organs were collected for *ex vivo* imaging (n = 3). As shown in Fig. 4A, no fluorescence was detected in the aortic arch for either the control or the Cy7.5 groups, whereas strong fluorescence signals were observed

Open Access Article. Published on 07 Caxah Alsa 2025. Downloaded on 06/05/2026 3:37:14 AM.
This article is licensed under a Creative Commons Attribution-NonCommercial 3.0 Unported Licence.

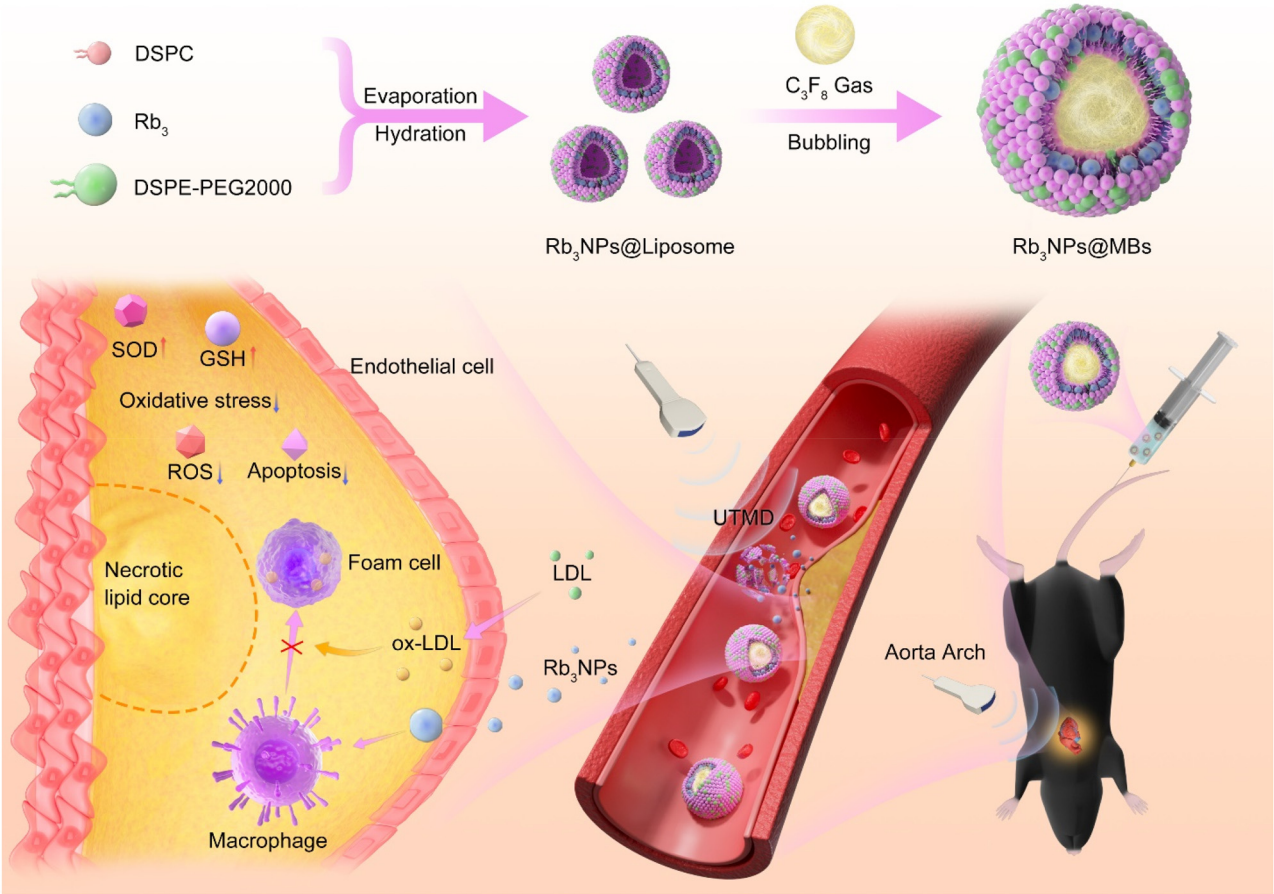

Scheme 1 The scheme of Rb_3NPs@MBs combined with UTMD for the targeted treatment of atherosclerosis. The Rb_3NPs@MBs burst in the targeted aortic arch under the guidance of ultrasound, and the energy generated by the explosion promotes drug penetration into the plaque, reduces the degree of oxidative stress in the plaque, decreases ROS, and upregulates the oxidation factors SOD and GSH, reduces the apoptosis of endothelial cells and the formation of foam cells, and ultimately reduces the plaque area and increases the stability of the plaque.

in the aortic arch of the Cy7.5@MBs + UTMD group. This conclusion was also verified by fluorescent section staining of the aortic arch (Fig. S8†). After 24 hours of circulation, fluorescence imaging of the major organs revealed that, in the Cy7.5 group, the liver exhibited the highest fluorescence intensity, whereas the Cy7.5@MBs + UTMD group showed minimal fluorescence in both the liver and the lungs (Fig. 4B).

Moreover, the overall fluorescence intensity in these organs was substantially lower than that in the Cy7.5 group. These findings suggest reduced hepatic retention of Cy7.5 in the Cy7.5@MBs + UTMD group, while residual fluorescence in the lungs confirms that microbubbles with small diameters can be metabolized *via* pulmonary clearance. Notably, the fluorescence indicated that UTMD successfully concentrated Cy7.5 at the ultrasound-targeted site and demonstrated the feasibility of this targeted delivery approach to overcome blood circulation.

3.6 Rb_3NPs@MBs in combination with UTMD targeted reduction of arterial plaques in AS mice

Apolipoprotein E knockout ($ApoE^{-/-}$) mice, also referred to as APOE-deficient mice, are widely recognized as a classical model for investigating AS.[55,56] Accordingly, five- to six-week-old $ApoE^{-/-}$ mice were maintained on a high-fat diet for 12 weeks to establish an AS model. In this study, simvastatin (SV) was selected as the positive control drug, given that statins remain the first-line therapy for AS. Additionally, to confirm that any therapeutic benefit did not result solely from the mechanical effects of MBs under ultrasound disruption, an MB-only group was included. Thus, C57BL/6 mice were assigned to the control group, whereas AS mice were allocated to the following groups, each containing eight animals: model, MBs + UTMD, SV, Rb_3NPs, and Rb_3NPs@MBs + UTMD. After 12 weeks of high-fat feeding, treatments were initiated, and following two weeks of intervention, the mice were euthanized for subsequent analyses (Fig. 6A).

3.6.1 Oil red O staining of aortas. Oil red O staining was performed on the entire aorta. Under the same dose and treatment frequency, the Rb_3NPs@MBs + UTMD group exhibited the smallest plaque area in the whole aorta, followed by the Rb_3NPs group. By contrast, the plaque areas in the MBs + UTMD group and the SV group did not significantly differ from the model group (Fig. 6B and D). Further analysis of the

 This journal is © The Royal Society of Chemistry 2025

Open Access Article. Published on 07 Caxah Alsa 2025. Downloaded on 06/05/2026 3:37:14 AM.
This article is licensed under a Creative Commons Attribution-NonCommercial 3.0 Unported Licence.

aortic arch, where UTMD was targeted, showed no difference in plaque area between the Rb_3NPs group and the model group, whereas the Rb_3NPs@MBs + UTMD group displayed a marked reduction in plaque area relative to both the model and Rb_3NPs groups (Fig. 6C and D). Hence, oil red O analysis for both the aorta and the aortic arch demonstrated that Rb_3NPs@MBs + UTMD specifically reduced the plaque area in the targeted region and exhibited stronger anti-atherosclerotic efficacy compared with Rb_3NPs alone, with a targeting efficiency of 31.9%.

3.6.2 Evaluation of serum inflammatory factors, oxidative stress, and lipids. AS is a systemic inflammatory disease, and quantifying inflammatory factors helps determine disease severity. Enzyme-linked immunosorbent assay (ELISA) results showed that IL-6 levels were significantly lower in the Rb_3NPs@MBs + UTMD group than in the model group, with a more pronounced decrease than in the Rb_3NPs group. Concurrently, TGF-β levels in the Rb_3NPs@MBs + UTMD group were significantly higher than those in the model group (Fig. 6E). Taken together, these findings reinforce the anti-inflammatory effects of Rb_3NPs@MBs + UTMD on AS.

SOD and GSH are key intracellular antioxidants, whereas malondialdehyde (MDA), a lipid peroxidation byproduct, is an indicator of oxidative stress. Biochemical assays demonstrated that SOD and GSH concentrations in the Rb_3NPs@MBs + UTMD group were significantly elevated compared with the model group, whereas MDA levels were markedly reduced, notably surpassing the reduction observed in the Rb_3NPs group (Fig. 6F). These results indicate that Rb_3NPs@MBs + UTMD ameliorates oxidative stress by increasing levels of the antioxidant factors SOD and GSH while decreasing MDA.

Next, to examine lipid profiles—a key reflection of abnormal lipid metabolism in AS—serum levels of triglycerides (TG), cholesterol (CHO), LDL, and HDL were measured. Levels of these lipids were significantly reduced in the Rb_3NPs@MBs + UTMD group compared with the model group (Fig. 6G), confirming that Rb_3NPs@MBs + UTMD can effectively modulate dyslipidaemia in AS.

3.6.3 Pathological staining of aortic plaques. Further pathological staining of the aortic plaques was performed to elucidate the direct effects of the treatment on plaque characteristics. VCAM-1, an endothelial adhesion molecule induced upon endothelial cell activation, is a pivotal factor in AS pathogenesis and a prime target for anti-AS therapies. Immunohistochemical staining showed that the VCAM-1-positive area was minimized in the Rb_3NPs@MBs + UTMD group (Fig. 7A), indicating significantly downregulated VCAM-1 expression. Oil red O staining of the aortic valve plaques revealed that the Rb_3NPs@MBs + UTMD group exhibited the smallest positively stained area (Fig. 7B), suggesting a notable reduction in plaque size following treatment. Masson staining demonstrated a higher proportion of blue-stained collagen in the plaques of the Rb_3NPs@MBs + UTMD group, indicative of enhanced plaque stability. HE staining likewise confirmed the reduced aortic root plaque area under Rb_3NPs@MBs + UTMD treatment.

Collectively, these data demonstrate that Rb_3NPs@MBs + UTMD successfully released the drug at the aortic arch targeted by ultrasound, thereby reducing local plaque burden, downregulating VCAM-1 expression, mitigating inflammation, and lowering both lipid and oxidative stress levels in treated mice.

4. Discussion and conclusions

In this study, we developed a novel ultrasound-visualized drug delivery system, termed Rb_3NPs@MBs, using saponin Rb_3. Both *in vitro* and *in vivo* experiments demonstrated that the combination of Rb_3NPs@MBs with UTMD effectively alleviated arterial plaques in AS.

Firstly, we successfully prepared microbubbles with a diameter of about 1.70 μm, and the Rb_3NPs@MBs were uniformly dispersed with good properties. The results of cellular uptake indicate that the mechanism of UTMD promoting cellular uptake of drugs is feasible (Fig. 2). Then at the cellular level, a CCK-8 assay confirmed that Rb_3NPs@MBs in conjunction with UTMD (1–100 μg ml^{-1}) did not compromise cell viability in both HUVECs and RAW264.7 cells. Following this screening, 10 μg ml^{-1} was chosen as the optimal *in vitro* concentration based on confocal microscopy analyses (Fig. 3A–C). Subsequent experiments indicated that Rb_3NPs@MBs reduced Dil-ox-LDL uptake in RAW264.7 cells, thereby inhibiting foam cell formation (Fig. 3D and E). In addition, flow cytometry revealed that Rb_3NPs@MBs suppressed HUVEC apoptosis (Fig. 3F and G). To investigate whether these beneficial effects were mediated through modulation of oxidative stress, we evaluated the mitochondrial membrane potential (*via* JC-1 staining) in HUVECs, measured ROS levels in RAW264.7 cells, and quantified key antioxidant factors (SOD and GSH) (Fig. 4). The results showed that Rb_3NPs@MBs preserved mitochondrial membrane potential in HUVECs, mitigated mitochondrial damage and ROS generation, and reduced ROS levels in RAW264.7 cells. Moreover, Rb_3NPs@MBs therapy elevated both SOD and GSH in endothelial cells and macrophages. Thus, Rb_3NPs@MBs inhibited early pathological events in AS, primarily by decreasing intracellular oxidative stress.

Because the aortic arch is predisposed to plaque formation (due to its angulation, increased branching, and abnormal shear forces),[57] we selected it as the primary target for UTMD-mediated drug delivery *in vivo*. *In vivo* imaging of small animals confirmed that UTMD overcame blood flow constraints, facilitated traversal of the endothelial barrier, and effectively accumulated Cy7.5 in the targeted aortic arch (Fig. 5A). $ApoE^{-/-}$ mice were treated for two weeks. Notably, the MBs + UTMD and SV groups did not show significant differences in biochemical indices or plaque burden relative to untreated AS controls (model group). Although Rb_3NPs alone reduced total plaque area in the aorta, its effect on the aortic arch, where the plaque was most advanced, remained limited. In contrast, Rb_3NPs@MBs + UTMD not only effectively reduced the overall plaque burden in the aorta but also signifi-

Open Access Article. Published on 07 Caxah Alsa 2025. Downloaded on 06/05/2026 3:37:14 AM.
This article is licensed under a Creative Commons Attribution-NonCommercial 3.0 Unported Licence.

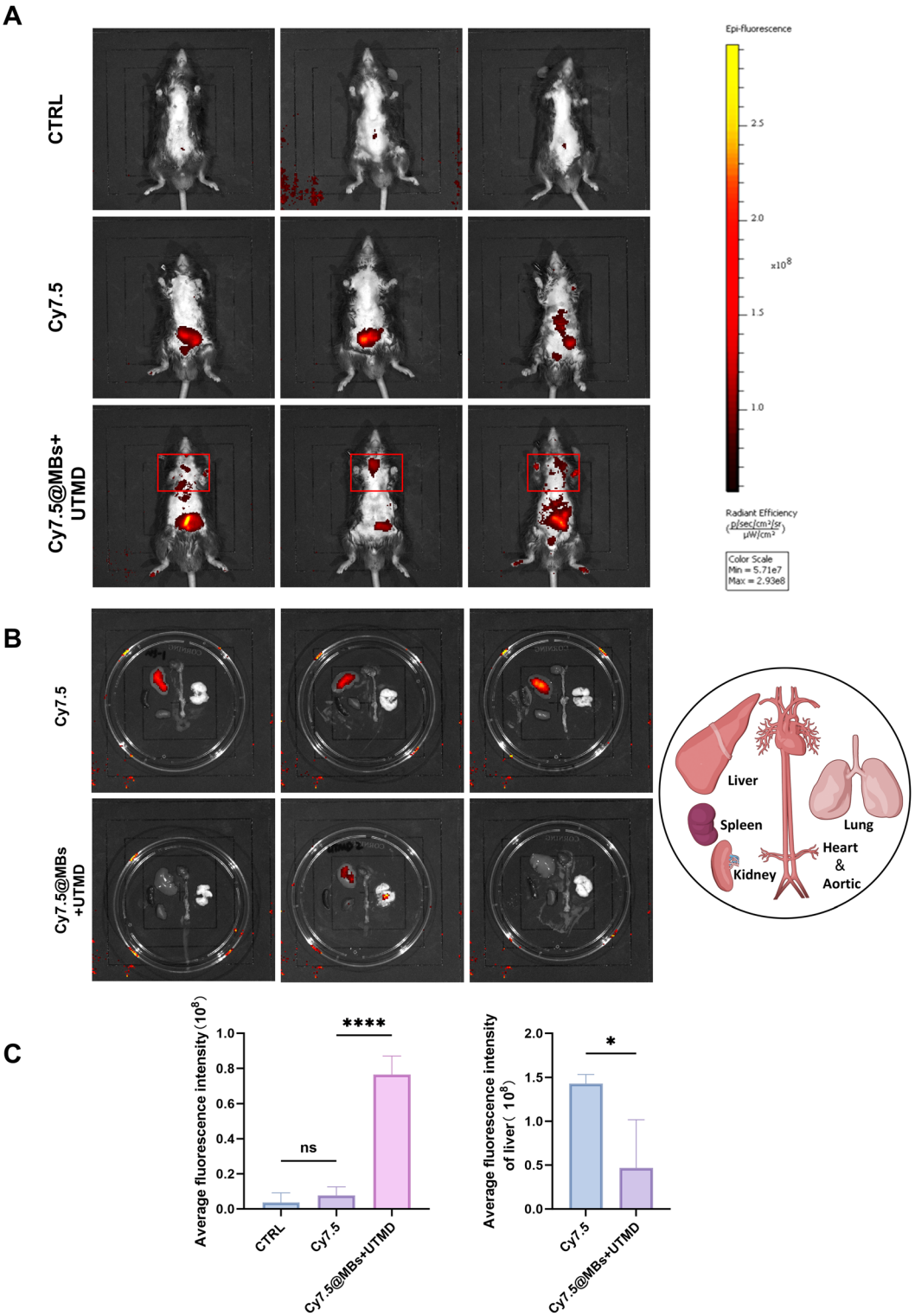

Fig. 5 Biodistribution of microbubbles combined with UTMD *in vivo* (n = 3). (A) *In vivo* fluorescence imaging of mice after UTMD (1 h). Color scale: min = 5.71 × 10^7, max = 2.93 × 10^8. (B) Fluorescence imaging of the mouse liver, spleen, lungs, kidneys, heart, and aorta after 24 h. Color scale: min = 1.12 × 10^8, max = 1.68 × 10^8. (C) Fluorescence quantitative analysis of (A) and (B) (n = 3).

cantly diminished plaques in the targeted aortic arch (Fig. 6B–D). The combination therapy simultaneously lowered inflammatory markers, oxidative stress, and lipid levels in AS mice (Fig. 6E–G). Pathological assessments of aortic valve plaques demonstrated that Rb_3NPs@MBs + UTMD reduced VCAM-1 expression, decreased lipid accumulation, increased plaque

 This journal is © The Royal Society of Chemistry 2025

Open Access Article. Published on 07 Caxah Alsa 2025. Downloaded on 06/05/2026 3:37:14 AM.
This article is licensed under a Creative Commons Attribution-NonCommercial 3.0 Unported Licence.

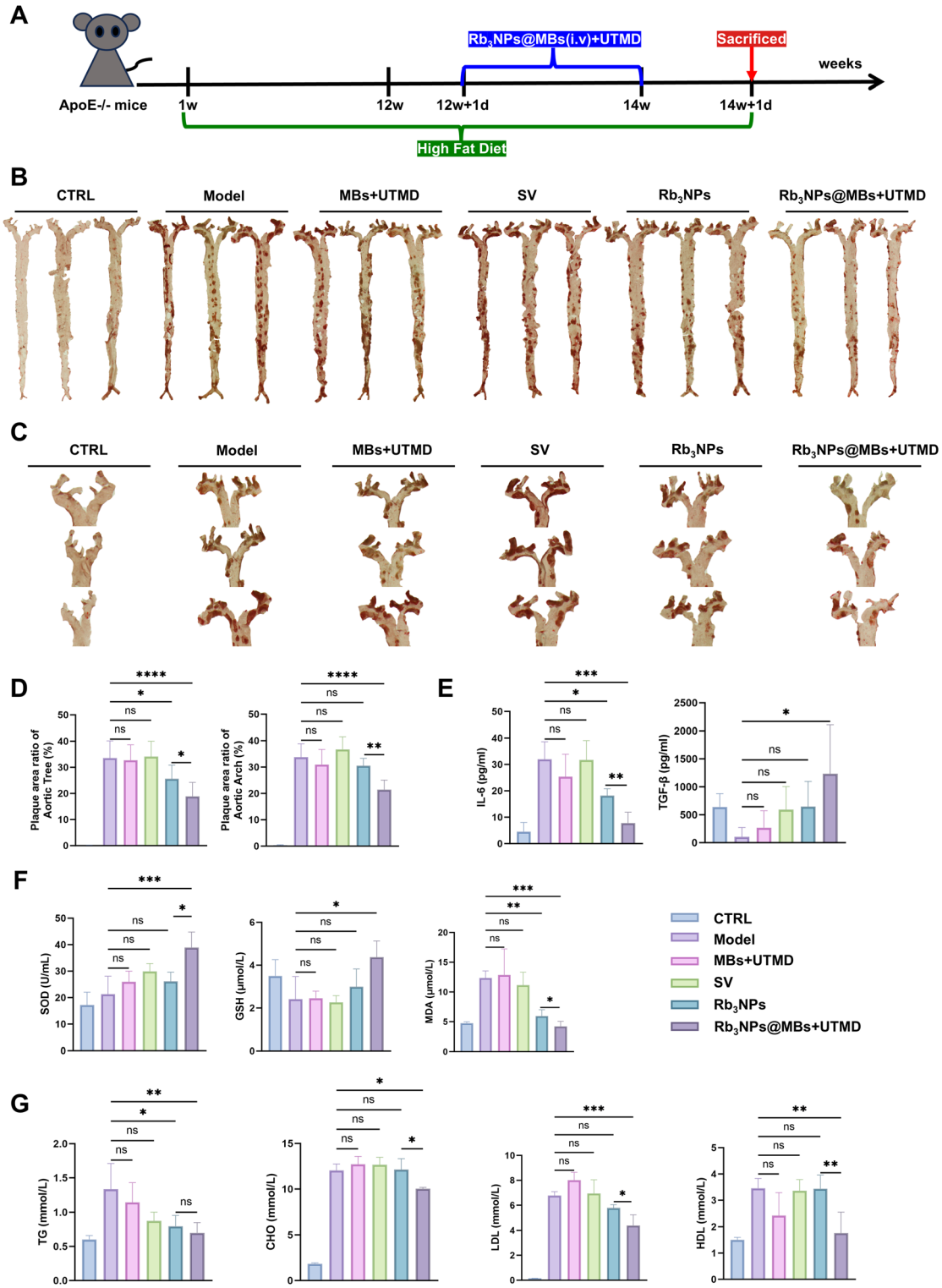

Fig. 6 Rb_3NPs@MBs in combination with UTMD targeted reduction of arterial plaque in AS mice. (A) Schematic diagram of the treatment cycle of mice (n = 8). (B) Aortic tree oil red O staining (n = 8). (C) Oil red O staining of aortic arch in mice. (D) Quantitative analysis of (B) & (C). (E) ELISA results of IL-6 and TGF-β in mouse serum (n = 5). (F) The biochemical detection results of oxidative stress factors SOD, GSH, and MDA in mouse plasma (n = 5). (G) Results of biochemical measurements of lipid levels of TG, CHO, LDL, and HDL in mouse serum (n = 5).

collagen content, and diminished plaque area, thereby corroborating its enhanced therapeutic efficacy (Fig. 7). Together, these results suggest that Rb_3NPs@MBs with UTMD can effectively deliver the drug to the targeted aortic arch, reduce plaque formation, and improve pathological indices relevant to AS.

Open Access Article. Published on 07 Caxah Alsa 2025. Downloaded on 06/05/2026 3:37:14 AM.
This article is licensed under a Creative Commons Attribution-NonCommercial 3.0 Unported Licence.

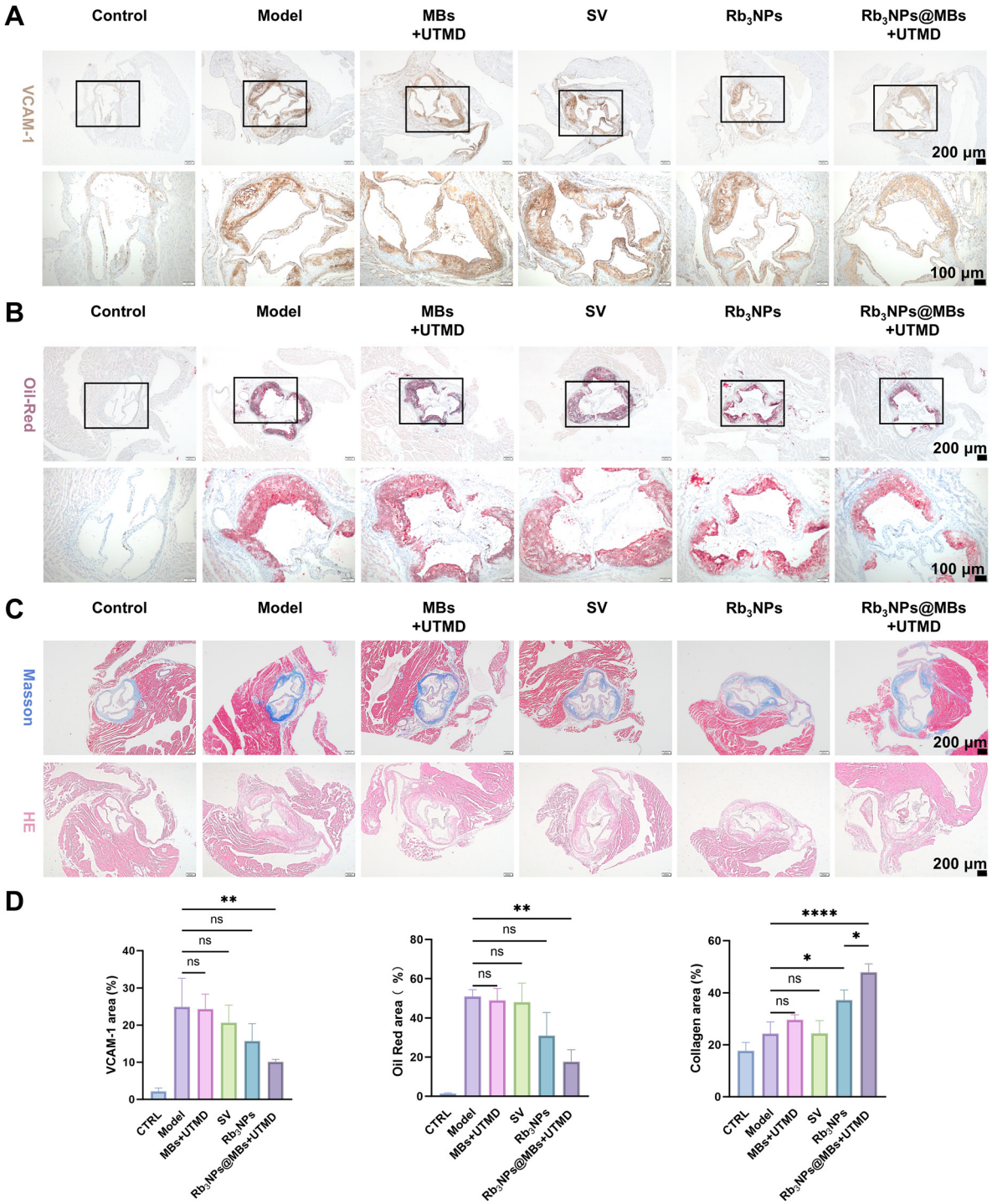

Fig. 7 Results of pathological sections of mouse aortic valves (n = 3). (A) Histochemical staining for VCAM-1 in sections of mouse aortic valves (first row: scale bar = 200 μm, second row: scale bar = 100 μm). (B) Oil red O staining of sections of mouse aortic valves (first row: scale bar = 200 μm, second row: scale bar = 100 μm). (C) Masson staining and HE staining of mouse aortic valve sections (scale bar = 200 μm). (D) The quantified results of VCAM-1 histochemical staining, oil red O staining and Masson staining.

In vitro, we observed that there was no significant difference between the Rb_3NPs@MBs + UTMD group and the Rb_3NPs group in RAW264.7 cells. Combined with the results of cellular uptake, we believe that the mechanism of ultrasound promoting drug uptake in RAW264.7 cells is also applicable, and the therapeutic effect is not obvious mainly because the active uptake of Rb_3NPs by cells also increases with time, accumulating to a level comparable to that of the Rb_3NPs@MBs + UTMD group at 24 h. Therefore, the final intracellular drug concentration was not significantly different between the two groups.

 This journal is © The Royal Society of Chemistry 2025

Open Access Article. Published on 07 Caxah Alsa 2025. Downloaded on 06/05/2026 3:37:14 AM.
This article is licensed under a Creative Commons Attribution-NonCommercial 3.0 Unported Licence.

This phenomenon may be related to the high affinity of macrophages for fat-soluble drugs, and further research is needed in the future. However, *in vitro* models cannot fully replicate the complexity of *in vivo* pathophysiology, and our *in vivo* results confirmed that Rb_3NPs@MBs combined with UTMD outperformed Rb_3NPs alone.

In conclusion, we successfully constructed a targeted drug delivery system—Rb_3NPs@MBs with UTMD—that demonstrated feasibility, efficacy, and safety in both *in vitro* and *in vivo* models. These findings highlight its potential for clinical application as a promising therapeutic strategy for AS. Ongoing research will aim to further optimize this system and evaluate its effectiveness in diverse AS models and clinical settings.

Author contributions

Manuscript drafting, data curation, investigation, and visualization: Chunting Zhong, Xiaoting Yang, Jianhua Bai, Yiran Ji, Xiao Tan, Xiaoyu Chen and Lijun Xing; methodology, validation, and project administration: Bingxuan Xu and Dianhuan Tan; *in vitro* experiments: Chunting Zhong and Jianhua Bai; *in vivo* imaging experiments: Chunting Zhong; *in vivo* experiments: Chunting Zhong, Xiaoting Yang, Jianhua Bai, Yiran Ji, Xiao Tan and Xiaoyu Chen; study design and conceptualization: Tingting Zheng; supplementary experimental data: Chunting Zhong, Jianhua Bai and Xiaoting Yang; resources and funding acquisition: Yun Chen and Tingting Zheng; supervision and manuscript editing: Tingting Zheng. All authors have approved the manuscript and agreed to its submission to *Biomaterials Science*.

Data availability

The data supporting this article have been included as part of the ESI.†

Conflicts of interest

There are no conflicts to declare.

Acknowledgements

This work was financially supported by the following: YC received financial support from grant no. KXCFZ202002011010487, JCYJ20210324131402008 and ZDSYS201504301045406. TZ received financial support from grant no. 2022A1515010986 and 2022A1515010296. All authors received financial support from grant no. SZSM202111011 and SZXK051.

References

1 V. Junaid, A. M. K. Minhas, M. Inam, C. Hinkamp, K. M. Talha, C. Meloche, S. Sheikh, A. Khoja, C. Krittanawong, E. M. Vaughan, D. K. Kalra, L. Slipczuk and S. S. Virani, *Curr. Atheroscler. Rep.*, 2024, **27**, 14.
2 P. Libby, J. E. Buring, L. Badimon, G. K. Hansson, J. Deanfield, M. S. Bittencourt, L. Tokgözoğlu and E. F. Lewis, *Nat. Rev. Dis. Primers*, 2019, **5**, 56.
3 L.-L. Bu, H.-H. Yuan, L.-L. Xie, M.-H. Guo, D.-F. Liao and X.-L. Zheng, *Int. J. Mol. Sci.*, 2023, **24**, 15160.
4 S. Jebari-Benslaiman, U. Galicia-García, A. Larrea-Sebal, J. R. Olaetxea, I. Alloza, K. Vandenbroeck, A. Benito-Vicente and C. Martín, *Int. J. Mol. Sci.*, 2022, **23**, 3346.
5 E. Niki, *Free Radicals Biol. Med.*, 2018, **120**, 425–440.
6 S. Zhong, L. Li, X. Shen, Q. Li, W. Xu, X. Wang, Y. Tao and H. Yin, *Free Radicals Biol. Med.*, 2019, **144**, 266–278.
7 Y. Li, M. Zhou, H. Li, C. Dai, L. Yin, C. Liu, Y. Li, E. Zhang, X. Dong, H. Ji and Q. Hu, *Eur. Heart J.*, 2024, **45**, 268–283.
8 L. Zhu, Y. Zhong, M. Yan, S. Ni, X. Zhao, S. Wu, G. Wang, K. Zhang, Q. Chi, X. Qin, C. Li, X. Huang and W. Wu, *ACS Appl. Mater. Interfaces*, 2024, **16**, 32027–32044.
9 P. Libby, *Nature*, 2021, **592**, 524–533.
10 P. Marchio, S. Guerra-Ojeda, J. M. Vila, M. Aldasoro, V. M. Victor and M. D. Mauricio, *Oxid. Med. Cell. Longevity*, 2019, **2019**, 1–32.
11 H. Ait-Oufella and P. Libby, *Arterioscler., Thromb., Vasc. Biol.*, 2024, **44**, 1899–1905.
12 X. Zhang, F. Centurion, A. Misra, S. Patel and Z. Gu, *Adv. Drug Delivery Rev.*, 2023, **194**, 114709.
13 L. H. Opie, *Trends Cardiovasc. Med.*, 2015, **25**, 216–225.
14 C. P. Cannon, *Eur. Heart J.*, 2019, **40**, 3526–3528.
15 A. Ajoolabady, D. Pratico, M. Mazidi, I. G. Davies, G. Y. H. Lip, N. Seidah, P. Libby, G. Kroemer and J. Ren, *Metabolism*, 2025, **163**, 156064.
16 P. M. Ridker, B. M. Everett, T. Thuren, J. G. MacFadyen, W. H. Chang, C. Ballantyne, F. Fonseca, J. Nicolau, W. Koenig, S. D. Anker, J. J. P. Kastelein, J. H. Cornel, P. Pais, D. Pella, J. Genest, R. Cifkova, A. Lorenzatti, T. Forster, Z. Kobalava, L. Vida-Simiti, M. Flather, H. Shimokawa, H. Ogawa, M. Dellborg, P. R. F. Rossi, R. P. T. Troquay, P. Libby and R. J. Glynn, *N. Engl. J. Med.*, 2017, **377**, 1119–1131.
17 M. A. Potenza, M. Montagnani, L. Santacroce, I. A. Charitos and L. Bottalico, *J. Ginseng Res.*, 2023, **47**, 359–365.
18 W. Fan, Y. Huang, H. Zheng, S. Li, Z. Li, L. Yuan, X. Cheng, C. He and J. Sun, *Biomed. Pharmacother.*, 2020, **132**, 110915.
19 J. Chen, X. Wei, Q. Zhang, Y. Wu, G. Xia, H. Xia, L. Wang, H. Shang and S. Lin, *Acta Pharm. Sin. B*, 2023, **13**, 1919–1955.
20 W. Jin, C. Li, S. Yang, S. Song, W. Hou, Y. Song and Q. Du, *Front. Pharmacol.*, 2023, **14**, 1166898.
21 S.-J. Oh, Y. Oh, I. W. Ryu, K. Kim and C.-J. Lim, *Biosci., Biotechnol., Biochem.*, 2016, **80**, 95–103.

Open Access Article. Published on 07 Caxah Alsa 2025. Downloaded on 06/05/2026 3:37:14 AM.
This article is licensed under a Creative Commons Attribution-NonCommercial 3.0 Unported Licence.

22 X. Chen, Q. Wang, M. Shao, L. Ma, D. Guo, Y. Wu, P. Gao, X. Wang, W. Li, C. Li and Y. Wang, *Biomed. Pharmacother.*, 2019, **120**, 109487.
23 T. Dai, W. He, C. Yao, X. Ma, W. Ren, Y. Mai and A. Wu, *Biomater. Sci.*, 2020, **8**, 3784–3799.
24 Y. Zhang, H. Ji, O. Qiao, Z. Li, L. Pecoraro, X. Zhang, X. Han, W. Wang, X. Zhang, S. Man, J. Wang, X. Li, C. Liu, L. Huang and W. Gao, *Biomed. Pharmacother.*, 2021, **139**, 111630.
25 S. Lu, P. Zhao, Y. Deng and Y. Liu, *Pharmaceutics*, 2022, **14**, 480.
26 W. He, X. Xing, X. Wang, D. Wu, W. Wu, J. Guo and S. Mitragotri, *Adv. Funct. Mater.*, 2019, **11**, 1855–1863.
27 S. Huo, P. Zhao, Z. Shi, M. Zou, X. Yang, E. Warszawik, M. Loznik, R. Göstl and A. Herrmann, *Nat. Chem.*, 2021, **13**, 131–139.
28 Q. Deng, J. Mi, J. Dong, Y. Chen, L. Chen, J. He and J. Zhou, *ACS Nano*, 2022, **17**, 263–274.
29 W. Guo, S. Huang, J. An, J. Zhang, F. Dong, J. Dang and J. Zhang, *ACS Appl. Mater. Interfaces*, 2022, **14**, 50664–50676.
30 X. Wang, F. Li, J. Zhang, L. Guo, M. Shang, X. Sun, S. Xiao, D. Shi, D. Meng, Y. Zhao, C. Jiang and J. Li, *J. Controlled Release*, 2024, **367**, 45–60.
31 H. Yang, Y. Sun, J. Wei, L. Xu, Y. Tang, L. Yang, X. Zhang and Y. Lu, *Biomed. Pharmacother.*, 2019, **118**, 109161.
32 A. Bouakaz and J. Escoffre, *Adv. Drug Delivery Rev.*, 2024, **206**, 115199.
33 W. Wei, Y. Wang, Z. Wang and X. Duan, *TrAC, Trends Anal. Chem.*, 2023, **160**, 116958.
34 Y. Yang, Q. Li, X. Guo, J. Tu and D. Zhang, *Ultrason. Sonochem.*, 2020, **67**, 105096.
35 S. Keller, M. Bruce and M. A. Averkiou, *Ultrasound Med. Biol.*, 2019, **45**, 833–845.
36 S. M. Chowdhury, L. Abou-Elkacem, T. Lee, J. Dahl and A. M. Lutz, *J. Controlled Release*, 2020, **326**, 75–90.
37 I. Lentacker, I. De Cock, R. Deckers, S. C. De Smedt and C. T. W. Moonen, *Adv. Drug Delivery Rev.*, 2014, **72**, 49–64.
38 I. De Cock, E. Zagato, K. Braeckmans, Y. Luan, N. de Jong, S. C. De Smedt and I. Lentacker, *J. Controlled Release*, 2015, **197**, 20–28.
39 B. van Elburg, J. Deprez, M. van den Broek, S. C. De Smedt, M. Versluis, G. Lajoinie, I. Lentacker and T. Segers, *J. Controlled Release*, 2023, **363**, 747–755.
40 K.-H. Song, A. C. Fan, J. T. Brlansky, T. Trudeau, A. Gutierrez-Hartmann, M. L. Calvisi and M. A. Borden, *Theranostics*, 2015, **5**, 1419–1427.
41 M. A. O'Reilly, *Science*, 2024, **385**, eadp7206.
42 Z. Zhang, B. Xu, T. Lv, Y. Shi, M. Wang, D. Hu, A. Hu, P. Li, S. Lin, S. Zhang, R. Yao, L. Luo, L. Wang, Y. Zhang, Y. Han, H. Hu, X. Shuai, J. Shi, Y. Chen and T. Zheng, *Adv. Ther.*, 2023, **6**, 2300056.
43 L. Duan, L. Yang, J. Jin, F. Yang, D. Liu, K. Hu, Q. Wang, Y. Yue and N. Gu, *Theranostics*, 2020, **10**, 462–483.
44 S. Liu, Y. Zhang, Y. Liu, W. Wang, S. Gao, W. Yuan, Z. Sun, L. Liu and C. Wang, *Br. J. Cancer*, 2022, **128**, 715–725.
45 X. Li, S. Guo, T. Xu, X. He, Y. Sun, X. Chen, S. Cao, X. Si, W. Liao, Y. Liao, Y. Han and J. Bin, *Theranostics*, 2020, **10**, 2522–2537.
46 B. G. Brown and X.-Q. Zhao, *J. Am. Coll. Cardiol.*, 2007, **49**, 933–938.
47 H. Yuan, H. Hu, J. Sun, M. Shi, H. Yu, C. Li, Y. U. Sun, Z. Yang and R. M. Hoffman, *In Vivo*, 2018, **32**, 1025–1032.
48 F. Liu, Y. Mao, J. Yan, Y. Sun, Z. Xie, F. Li, F. Yan, H. Zhang and P. Zhang, *Research*, 2022, **2022**, 9830627.
49 J. Pazzi and A. B. Subramaniam, *J. Colloid Interface Sci.*, 2024, **661**, 1033–1045.
50 L. Fournier, T. de La Taille and C. Chauvierre, *Biomaterials*, 2023, **294**, 122025.
51 Y. Wen, Y. Ji, S. Zhang, B. Xu, S. Sun, Y. Chen, X. Shuai and T. Zheng, *Aging*, 2024, **16**, 10784–10798.
52 Z. He, W. Chen, K. Hu, Y. Luo, W. Zeng, X. He, T. Li, J. Ouyang, Y. Li, L. Xie, Y. Zhang, Q. Xu, S. Yang, M. Guo, W. Zou, Y. Li, L. Huang, L. Chen, X. Zhang, Q. Saiding, R. Wang, M.-R. Zhang, N. Kong, T. Xie, X. Song and W. Tao, *Nat. Nanotechnol.*, 2024, **19**, 1386–1398.
53 Z.-C. Wang, K.-M. Niu, Y.-J. Wu, K.-R. Du, L.-W. Qi, Y.-B. Zhou and H.-J. Sun, *Cell Death Dis.*, 2022, **13**, 824.
54 R. Cannella, G. Pilato, M. Mazzola and T. V. Bartolotta, *Radiol. Med.*, 2023, **128**, 1023–1034.
55 C. Lane-Donovan, W. M. Wong, M. S. Durakoglugil, C. R. Wasser, S. Jiang, X. Xian and J. Herz, *J. Neurosci.*, 2016, **36**, 10141–10150.
56 E. Asimakidou, E. N. Saipuljumri, C. H. Lo and J. Zeng, *Neural Regener. Res.*, 2024, **20**, 1069–1076.
57 P. Libby and G. K. Hansson, *Circ. Res.*, 2015, **116**, 307–311.

This journal is © The Royal Society of Chemistry 2025